Editors' Suggestion | Featured in Physics

Quantum-Coherent Light-Electron Interaction in a Scanning Electron Microscope

R. Shiloh,[*,†] T. Chlouba,[*,‡] and P. Hommelhoff[§]
Physics Department, Friedrich-Alexander-Universität Erlangen-Nürnberg (FAU), Staudtstraße 1, 91058 Erlangen, Germany

(Received 10 November 2021; revised 21 January 2022; accepted 29 March 2022; published 6 June 2022)

The last two decades experimentally affirmed the quantum nature of free electron wave packets by the rapid development of transmission electron microscopes into ultrafast, quantum-coherent systems. So far, all experiments were restricted to the bounds of transmission electron microscopes enabling one or two photon-electron interaction sites. We show the quantum coherent coupling between electrons and light in a scanning electron microscope, at unprecedentedly low, subrelativistic energies down to 10.4 keV. These microscopes not only afford the yet-unexplored energies from ~0.5 to 30 keV providing the optimum electron-light coupling efficiency, but also offer spacious and easily configurable experimental chambers for extended, cascaded optical set ups, potentially boasting thousands of photon-electron interaction sites. Our results make possible experiments in electron wave packet shaping, quantum computing, and spectral imaging with low-energy electrons.

DOI: 10.1103/PhysRevLett.128.235301

While transmission electron microscopes (TEMs) [1] are built to provide highly coherent electron beams for diffraction-based imaging methods [2], they are large and costly in terms of purchasing and maintenance. In contrast, scanning electron microscopes (SEMs) [3] are built to image surfaces based on scanning a small, focused electron beam over a sample, not requiring electron beam coherence or large beam energies (70–300 keV in TEMs), making the electron column more compact, the device easy to operate and more affordable. The different *modi operandi* lead to entirely different sample chamber geometries and placements: in a typical SEM, the sample chamber measures 30 cm across, whereas it is 3–7 mm in a TEM.

A new mode of imaging and photon-electron interaction was introduced more than a decade ago in TEMs: photon-induced near-field electron microscopy (PINEM) [4,5], which laid the foundation not only to a new ultrafast time-resolved electron imaging mode but also to breakthrough electron-light coupling [6–11] and, more recently, to extremely high coupling strengths using cavities, whispering-gallery modes, quasiphase matching, and microresonators [12–16].

In PINEM physics, a single electron wave packet and the light field exchange an integer number of photons in an inelastic interaction. In each photon exchange, the electron can absorb or emit one or more photons, which results in acceleration or deceleration of the electron. Multiples of such events are possible because the electron energy is several orders of magnitude larger than the net change the photon induces; however, a single exchange can still occur even at very low (<500 eV) energies (see the Appendix). While the underlying theory is well established [6,7,10,17], new predictions are still being made [17–21]. It revolves around the near-field interaction coupling constant, or PINEM field parameter g,

$$g(x,y) = \frac{e}{\hbar\omega}\int_{-\infty}^{\infty} E_z(x,y,z')e^{-iz'\omega/v}dz', \tag{1}$$

where e is the electric charge, $\hbar$ the reduced Planck constant, ω the central angular frequency of the laser field, E_z the complex optical electric field projection in the direction of the electron propagation $\hat{\mathbf{z}}$, and v the electron velocity. This expression is valid if the electron is measured after the interaction is finished, and is the Fourier transform of the electric field's z component with spatial frequency $q = \omega/v$. This implies that out of the many near-field wave vectors generated by the laser illuminating the sample, the electron coherently and most strongly interacts only with one component q. At TEM energies (fast electrons), q corresponds to low spatial frequencies, which decay farther away from the sample boundary, while at SEM energies (slow electrons), q corresponds to high near-field spatial frequencies that decay after a shorter distance. However, as discussed in great depth in Ref. [22] and investigated from first principles in Ref. [23], the photon-electron coupling strength can be several times stronger for slower electrons, because the lower spatial frequencies carry larger field amplitudes. Therefore, SEMs are better poised to reach the optimum photon-electron coupling in such experiments. Intriguingly, this argument also holds when considering the Smith-Purcell effect: the generation of photons by electrons moving next to material boundaries, and therefore the photon-electron coupling, is optimal for slower rather than faster electrons [24,25].

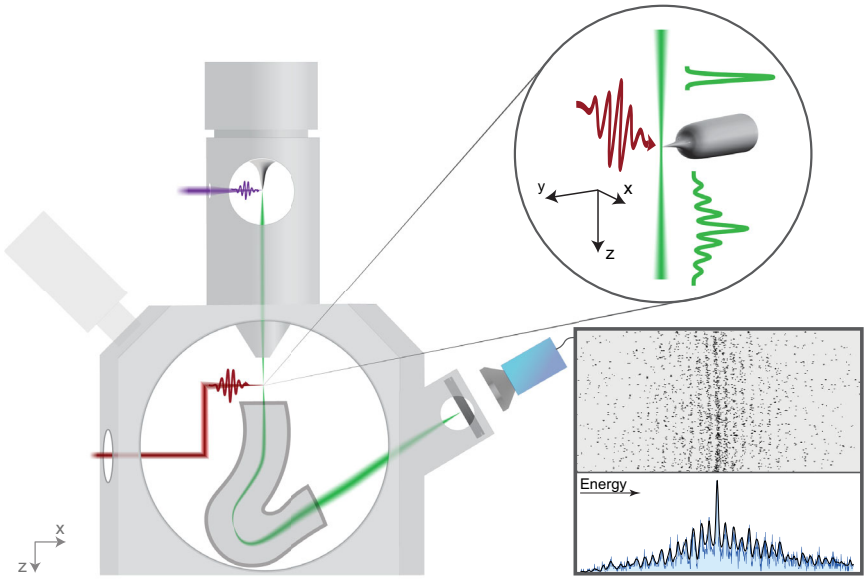

FIG. 1. Quantum coherent electron-light coupling in an ultrafast SEM. Electrons photoemitted by ultraviolet laser pulses (purple) propagate through the column of a commercial SEM. The electron beam (green) is focused close to a tungsten needle tip (inset), where it interacts with the optical near-field excited by 1030-nm laser pulses, coupled into the SEM through a CF-100 window in the SEM sample chamber. The aspherical focusing lens (not shown) is 25 mm away from the tip, inside of the chamber. Electron spectra are recorded with a home-built compact double-stage magnetic sector electron spectrometer based on the Omega filter, placed inside the SEM. The dispersion plane of the spectrometer is imaged onto a microchannel plate detector, whose phosphor screen is optically recorded from outside of the vacuum chamber with a CMOS camera. An example image (bottom right inset), where individual electron counts (black dots) and photon orders (vertical dotted lines) can be easily seen by the eye. The PINEM spectrum is obtained by integrating the camera image vertically [38]. The incoherently averaged experimental spectrum (black), with the raw, binned data (blue), show 24 PINEM orders, 12 on each side, the maximum we observed. A magnified version is available in Ref. [38].

Imaging using photon-electron interactions includes experimentally investigating the quantum nature and the response of nano-structures, molecules and atoms to incident light, mediated by the generated evanescent electromagnetic fields [26–28]. Examples of the fundamentals of electron-light coupling include attosecond quantum coherent control [8,11,29], quantum state reconstruction [30] and generation [31], attosecond pulse generation [30,32,33], and photon statistics reconstruction [16].

These remarkable demonstrations are all based on (i) steering and positioning of high quality electron beams with nanometer resolution—the core features of electron microscopes—and (ii) the ability to measure the electron's energy after its interaction with the optical near field, with a resolution better than the photon energy of the driving light field. In TEMs, this is straightforward because electron energy loss spectrometry (EELS) is a widely used measurement modality, so that the required spectral resolution can be achieved with standard, commercial EELS spectrometers. In contrast, this mode of imaging does not exist in normal SEM operation, which relies on signals detected from secondary or backscattered electrons, rather than transmitted electrons. Although an EELS spectrometer was first demonstrated in SEM in transmission mode by Khursheed *et al.* in 2003 [34], it was only recently that a commercially offered EELS detector was experimentally characterized in a SEM with a cold field emitter [35,36].

We equipped a commercial but significantly modified SEM with a specially designed, home-built compact high resolution magnetic spectrometer to introduce the required spectral energy resolution (Fig. 1). The design, based on an Omega energy filter [37], enables us to observe the coherent energy transfer between the exciting 1030 nm laser light (photon energy: 1.2 eV) and our subrelativistic electrons. We focus the laser beam on a tungsten needle tip to generate an optical near-field and measure the energy spectrum following the electron interaction.

Figure 1 shows a sketch of the experimental setup: an electron wave packet (green), released from the SEM emitter following photoexcitation by an ultraviolet laser pulse (purple) and accelerated to 17.4 keV, travels in the $\hat{\mathbf{z}}$ direction and interacts with the near field of the tungsten needle tip (Fig. 1 inset) aligned to the y axis. The near field is generated by a 1030 nm, 250 fs pulsed laser beam (dark red) propagating along the x axis. After the photon-electron interaction, the electron wave packet is dispersed in our photon energy-resolving spectrometer, the dispersion plane of which is imaged on a microchannel plate detector with phosphor screen, allowing single electron detection [38].

Figure 2 shows photon-resolved electron spectra. We focused the electron beam to various positions in close proximity of the needle tip, such that the beam samples the near field, and recorded a series of spectra (black line with

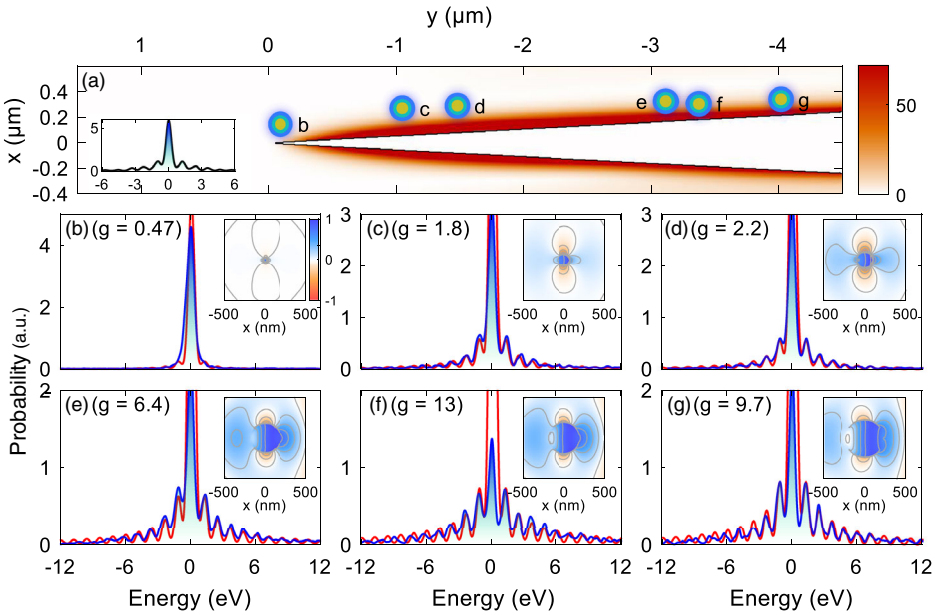

FIG. 2. PINEM spectra as function of position along the needle tip. (b)–(g) Six electron energy spectra at a central beam energy of 17.4 keV, recorded and matched to positions indicated by the colored circles in (a). The color scale in (a) shows a simulation of the near-field coupling parameter g. Spectrum (b) does not show photon orders, as expected for a beam not passing the optical near field of the tip. Spectrum (c) shows 3 photon orders on either side of the zero-loss peak, spectrum (d) 4, and up to 7 photon orders in spectrum (f). Experimental data are displayed by the blue curve and gradient; numerical results are in red. Clearly, the numerical results match the experimental data very well. The zero-loss peak height depends on the laser and electron pulse lengths, where the electron pulse was assumed infinite in time and ignored in the simulation; instead, the first positive simulated energy peak's amplitude was normalized to the experimental one. The circle's positions in (a) are found such that the incoherent average of the simulated PINEM spectra match the experimental ones best. For details, see text and Ref. [38]. In each panel (b)–(g), the simulated value of the coupling parameter g at the center of the electron beam spot is shown for maximum laser pulse strength, and an inset showing the cross section of the real part of the simulated normalized electric field in the y direction is shown; with increase of diameter comes a mix of dipole, quadrupole, and higher multipoles of the field, whereas initially the dipole is almost exclusively excited. The aspect ratio of each inset is 1 : 1. The inset in (a) was recorded with 10.4 keV electrons. Also at this low energy we observe 4 photon orders on each side.

blue background) at different locations along the tip axis [colored circles in Fig. 1(a)]. Both the number and amplitude of the photon orders vary as a function of electron beam position: if the electrons pass outside of the near field, no PINEM orders are observed (panel b). Steering the electron beam up the tip, we observe an increase in PINEM orders from 3 on each side (panel c) up to 7 (panel f). Simultaneously, the spectral amplitudes vary. Numerical simulation results (red) based on standard PINEM theory almost perfectly match these results: First, we calculate the near-field coupling parameter g of the needle tip from a 3D electromagnetic field simulation [Fig. 2(a)]. This simulation does not take into account other effects that might affect the spectra, such as electron energy loss by Smith Purcell radiation; indeed, a slightly enhanced signal towards energy loss is apparent in the measured data (blue curve and shade). Also, the mismatch between experiment and simulation of the central peak (zero energy deviation) is due to the electron pulse being at least 4 times as long as the laser pulse, hence, many electrons do not interact with the generated near fields and their energy is unchanged. The electron pulse length is not included in the simulation.

In each of the panels (b)–(g) in Fig. 2, we additionally included a cross section of the real part of the normalized electric field component along the electron propagation direction E_z. Clearly, when the cross-sectional diameter is very small, the field distribution around the needle tip is predominantly a dipole [panels (b)–(d)], while for larger diameters a mix of dipole, quadrupole, and higher multipoles is evident. The multipole composition, coupled with the distance from the needle-tip boundary, define the strength of the PINEM effect.

While a rigorous derivation must be made for a needle tip or a finite cylinder, we can understand this result by assuming an infinite cylinder and Mie theory: In the thin wire approximation [6] the near fields are calculated analytically to the first-order term by assuming that the cylinder radius a is much smaller than the incident laser wavelength (Rayleigh dipole approximation). The resulting electric field is

$$\vec{\mathbf{E}}(\vec{\mathbf{r}},t) \approx E_0 \chi_c \frac{a^2}{r^4} e^{-i\omega t}[-2xz\hat{\mathbf{x}} + (x^2 - z^2)\hat{\mathbf{z}}], \qquad (2)$$

where $\chi_c = (\tilde{n}^2 - 1)(\tilde{n}^2 + 1)^{-1}$ is the cylindrical susceptibility and $\tilde{n}$ the complex refractive index. E_0 is the

incident electric field amplitude polarized along $\hat{\mathbf{z}}$, and the cylinder is oriented along the $\hat{\mathbf{y}}$ direction. With this field, the interaction coupling constant g can be calculated from Eq. (1). Solving the time dependent Schrödinger equation yields the discrete probabilities P_n of exchange of n energy quanta between the electron wave packet and classical light field [6],

$$P_n = J_n^2(2|g|), \tag{3}$$

where J_n is the nth Bessel function of the first kind. The spectrum at $z \to \infty$, long after the interaction ceases, is a sum of evenly spaced delta distributions with weights P_n. These probabilities are used to match the numerical simulation to the experimental measurements in Fig. 2 (see also Ref. [38]).

Intriguingly, the number of PINEM orders observed here resembles those in a TEM under similar conditions, i.e., with an individual nano-object generating the near field [8]. The largest photon order number we observed was 12, corresponding to a modulated photon energy of 14.4 eV (inset of Fig. 1). Notably, we measured at least 4 photon orders at an energy as low as 10.4 keV [inset of Fig. 2(a)], which we expect is by no means the lower limit. Future work with improved electron current stability will allow longer measurement sessions and consequently better signal to noise ratio [38]. By focusing the electron probe to smaller dimensions, the near-fields sampling and accordingly the photon-electron coupling can be improved, yielding additional photon orders. Using high efficiency phase-matched coupling structures might allow measurement of thousands of PINEM orders as already observed with a TEM [42]. Most interestingly, specially designed structures and laser pulses can be engineered to shape the PINEM spectra [17]. Because of our single-electron detection efficiency, we can observe the buildup of the energy spectra on the detector in real-time (see Supplemental Material, movie [38]).

The main sample chamber volume of a standard SEM typically measures at least $20 \times 20 \times 20$ cm^3, versus the 3 mm^3 of a TEM. This offers a large flexibility in modifying the SEM chamber by installing large optical windows or electrical connections, and simplifying the coupling and extraction of signals from the vacuum chamber, a venture that can hardly be undertaken in a TEM. Furthermore, and even more important, a SEM can potentially accommodate many interaction locations for complex, cascaded quantum experimental schemes. A great practical advantage of a SEM is the convenience of using high numerical aperture optics (NA ≈ 1), which is challenging in a TEM. Also, an ultrafast SEM has reduced damage to sensitive specimen and materials [43,44], where an energy filtered scheme can provide key information on the sample otherwise hardly attainable [45]. Very recently, nanophotonic chips have been introduced to couple light and electrons efficiently [15,16]. With even longer versions, we foresee up to tens of thousands independent light-electron interaction sites, which might enable complex free electron-based quantum computing [46]. Today, quantum information systems use the interplay of light and matter fundamentally tied to the energy levels of bound electrons, so in bulk materials or gases. In contrast, systems based on free electrons provide a quantized energy ladder accessible in high-energy and ultrashort timescales. In Ref. [46], the authors discuss the feasibility and provide a framework for such a quantum information manipulation system, and explain how PINEM can be employed to demonstrate a full single qubit. A second, most important building block in that scheme is free-space propagation of the electrons. Several such blocks are required to implement qubit algebra, an experimental feat that may enjoy the spacious benefits of a photon-energy resolving SEM. With these abilities, such a SEM is perfectly staged for quantum-coherent experiments, including arbitrary electron wave function shaping [21]. Our feasibility demonstration of utilizing a SEM to perform such endeavors is a first invaluable step in this direction. Having access to the distribution of discrete energy levels of an electron wave packet, both in terms of manipulation and observation, is paramount to fundamental research in the quantum nature of matter, but also to future applications of quantum information and theory, and as a tool for ultrafast time-resolved electron imaging applications [47]. Finally, the ideal energy for various exciting future quantum-coherent electron-matter coupling experiments such as free electron bound electron interaction (FEBERI) [48] is in the range of a few keV [49,50], easily attainable with a SEM.

We acknowledge fruitful discussions with Professor Ido Kaminer and Professor Albert Polman. Funding was provided by the Gordon and Betty Moore Foundation (No. GBMF4744) and ERC Grant AccelOnChip (No. 884217) T. C. measured the data, R. S. designed and built the electron spectrometer, and performed the simulations. R. S. and T. C. analyzed the data. All authors contributed to the writing of the manuscript. P. H. supervised the experiment.

Appendix: Pinem electron-photon energy ratio approximation.—In the seminal PINEM theory paper by Park *et al.* [6], the authors assume that the electron energy is orders of magnitude larger than the interacting photon energy and proceed to approximate the critical angle Θ_c between the electron and photon, required to satisfy energy and momentum conservation (see equation 3 in Ref. [6]):

$$\cos(\Theta_c) = \frac{2\hbar\omega_p E_e + (\hbar\omega_p)^2 - (\hbar k_p c)^2}{2\hbar k_p c^2 p_e} \approx \frac{\bar{v}_p}{v_e}, \tag{A1}$$

where $\bar{v}_p = \omega_p/k_p$ is the phase velocity of the photon, $v_e = \partial E_e/\partial p_e = c^2 p_e/E_e$ is the electron velocity, and E_e

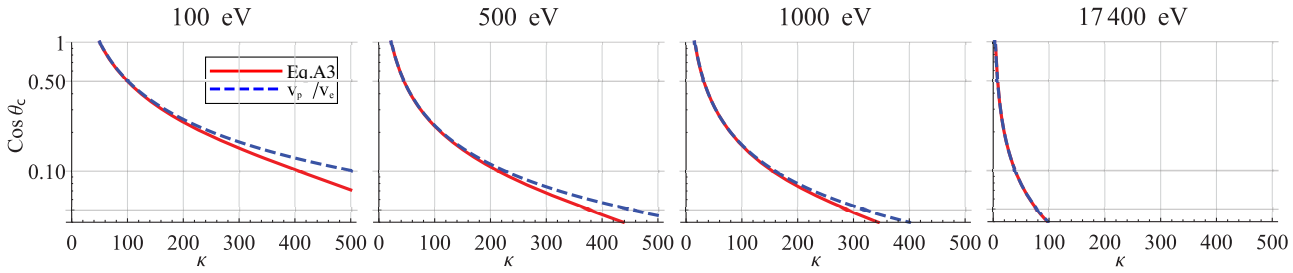

FIG. 3. Comparison of the full and approximated dependence of the critical angle required for conservation of the photon-electron interaction. The difference in the angle is quite small (as plotted on a semi-logarithmic scale), even for low (100 eV) electron energies, and requires state-of-the-art slow plasmons to observe a difference.

is the total energy of the electron. p_e is the electron's relativistic momentum and c is the speed of light in vacuum. ω_p and k_p are the angular frequency and wave number of the photon, respectively. A naturally poised question would be, at what electron energy does this approximation break?

In fact, the answer depends not only on the electron energy, but primarily on the nanostructure. In vacuum, the dispersion relation $\omega_p = ck_p$ holds. However, in PINEM physics the photon-electron interaction is mediated by a nanostructure, such that $\omega_p \sim k_p(v_p)$, which may be highly nonlinear. We can rewrite Eq. (3) without the approximation. After some algebra, we find that

$$\cos(\Theta_c) = \frac{\bar{v}_p}{v_e}\left(1 + \frac{\omega_p\hbar}{2E_e} - \frac{c^2\omega_p\hbar}{2E_e\bar{v}_p^2}\right). \tag{A2}$$

Since we are now interested in small kinetic energies (Lorentz factor $\gamma \approx 1$), we may approximate the total electron energy as $E_e = \gamma m_e c^2 \approx m_e c^2$, m_e the electron mass, and find that

$$\cos(\Theta_c) \approx \frac{\bar{v}_p}{v_e}\left(1 + \frac{\omega_p\hbar}{2m_e c^2} - \frac{\omega_p\hbar}{2m_e\bar{v}_p^2}\right). \tag{A3}$$

The second term in the parenthesis, assuming our photon wavelength of $\lambda = 1030$ nm, is of the order of 10^{-6} and negligible. The third term, however, is key: it includes the photon velocity, which contains the aforementioned dependence on the nanostructure ($\bar{v}_p \sim k_p^{-1}$). Plasmon polaritons have been previously shown to be slowed down even by a factor of 300 from the speed of light ($\bar{v}_p \approx c/300$) in graphene [51,52]. In the conventional, rather simple cases of metals, practical plasmon velocity ratios are of the order of 10. In Fig. 3, Eq. (A3) is plotted as a function of $\kappa = c/\bar{v}_p$ for different electron energies. Two qualitative conclusions arise: (i) with smaller electron energy, the near-field photons must be extraordinarily slowed down ($\kappa > \sim 50$ for 100 eV) in order to interact with the ultralow energy electrons; (ii) observable differences might only be seen with state-of-the-art slow plasmons and low electron energies (e.g., $\kappa > 300$ and 500 eV).

Incidentally, Talebi [23] looked into interaction of low-energy electrons ($\sim < 500$ eV) with photons employing a time-dependent Schrödinger-Maxwell simulation, and concluded again the importance of the structure size in this interaction; she also showed changes and asymmetry in the predicted PINEM spectrum and 2D angle-resolved energy spectrum. However, at present it is difficult to assess whether these would be observable in experiment, certainly requiring state-of-the-art experimental setup.

*R. S. and T. C. contributed equally to this work.
†roy.shiloh@fau.de
‡tomas.chlouba@fau.de
§peter.hommelhoff@fau.de

[1] M. Knoll and E. Ruska, Das Elektronenmikroskop, Z. Phys. **78**, 318 (1932).
[2] L. Reimer and H. Kohl, *Transmission Electron Microscopy* (Springer, New York, 2008).
[3] M. von Ardenne, Das Elektronen-Rastermikroskop, Z. Phys. **109**, 553 (1938).
[4] B. Barwick, D. J. Flannigan, and A. H. Zewail, Photon-induced near-field electron microscopy, Nature (London) **462**, 902 (2009).
[5] A. H. Zewail, Four-dimensional electron microscopy, Science **328**, 187 (2010).
[6] S. T. Park, M. Lin, and A. H. Zewail, Photon-induced near-field electron microscopy (PINEM): Theoretical and experimental, New J. Phys. **12**, 123028 (2010).
[7] F. J. García de Abajo, A. Asenjo-Garcia, and M. Kociak, Multiphoton absorption and emission by interaction of swift electrons with evanescent light fields, Nano Lett. **10**, 1859 (2010).
[8] A. Feist, K. E. Echternkamp, J. Schauss, S. V. Yalunin, S. Schäfer, and C. Ropers, Quantum coherent optical phase modulation in an ultrafast transmission electron microscope, Nature (London) **521**, 200 (2015).
[9] L. Piazza, T. T. A. Lummen, E. Quiñonez, Y. Murooka, B. W. Reed, B. Barwick, and F. Carbone, Simultaneous observation of the quantization and the interference pattern of a plasmonic near-field, Nat. Commun. **6**, 6407 (2015).

[10] F. J. García de Abajo, B. Barwick, and F. Carbone, Electron diffraction by plasmon waves, Phys. Rev. B **94**, 041404(R) (2016).
[11] G. M. Vanacore, I. Madan, G. Berruto, K. Wang, E. Pomarico, R. J. Lamb, D. McGrouther, I. Kaminer, B. Barwick, F. J. García de Abajo, and F. Carbone, Attosecond coherent control of free-electron wave functions using semi-infinite light fields, Nat. Commun. **9**, 2694 (2018).
[12] K. Wang, R. Dahan, M. Shentcis, Y. Kauffmann, A. Ben Hayun, O. Reinhardt, S. Tsesses, I. Kaminer, A. Ben Hayun, O. Reinhardt, S. Tsesses, and I. Kaminer, Coherent interaction between free electrons and a photonic cavity, Nature (London) **582**, 50 (2020).
[13] O. Kfir, H. Lourenço-Martins, G. Storeck, M. Sivis, T. R. Harvey, T. J. Kippenberg, A. Feist, and C. Ropers, Controlling free electrons with optical whispering-gallery modes, Nature (London) **582**, 46 (2020).
[14] R. Dahan, S. Nehemia, M. Shentcis, O. Reinhardt, Y. Adiv, X. Shi, O. Be'er, M. H. Lynch, Y. Kurman, K. Wang, and I. Kaminer, Resonant phase-matching between a light wave and a free-electron wavefunction, Nat. Phys. **16**, 1123 (2020).
[15] J.-W. Henke, A. S. Raja, A. Feist, G. Huang, G. Arend, Y. Yang, J. Kappert, R. N. Wang, M. Möller, J. Pan, J. Liu, O. Kfir, C. Ropers, and T. J. Kippenberg, Integrated photonics enables continuous-beam electron phase modulation, Nature (London) **600**, 653 (2021).
[16] R. Dahan, A. Gorlach, U. Haeusler, A. Karnieli, O. Eyal, P. Yousefi, M. Segev, A. Arie, G. Eisenstein, P. Hommelhoff, and I. Kaminer, Imprinting the quantum statistics of photons on free electrons, Science eabj7128 (2021).
[17] O. Reinhardt and I. Kaminer, Theory of shaping electron wavepackets with light, ACS Photonics **7**, 2859 (2020).
[18] A. Gover and Y. Pan, Dimension-dependent stimulated radiative interaction of a single electron quantum wavepacket, Phys. Lett. A **382**, 1550 (2018).
[19] Y. Pan and A. Gover, Spontaneous and stimulated radiative emission of modulated free-electron quantum wavepackets—semiclassical analysis, J. Phys. Commun. **2**, 115026 (2018).
[20] Y. Pan, B. Zhang, and A. Gover, Anomalous Photon-Induced Near-Field Electron Microscopy, Phys. Rev. Lett. **122**, 183204 (2019).
[21] A. Ben Hayun, O. Reinhardt, J. Nemirovsky, A. Karnieli, N. Rivera, and I. Kaminer, Shaping quantum photonic states using free electrons, Sci. Adv. **7**, eabe4270 (2021).
[22] M. Liebtrau, M. Sivis, A. Feist, H. Lourenço-Martins, N. Pazos-Pérez, R. A. Alvarez-Puebla, F. J. G. de Abajo, A. Polman, and C. Ropers, Spontaneous and stimulated electron–photon interactions in nanoscale plasmonic near fields, Light Sci. Appl. **10**, 82 (2021).
[23] N. Talebi, Strong Interaction of Slow Electrons with Near-Field Light Visited from First Principles, Phys. Rev. Lett. **125**, 080401 (2020).
[24] Y. Yang, A. Massuda, C. Roques-Carmes, S. E. Kooi, T. Christensen, S. G. Johnson, J. D. Joannopoulos, O. D. Miller, I. Kaminer, and M. Soljačić, Maximal spontaneous photon emission and energy loss from free electrons, Nat. Phys. **14**, 894 (2018).
[25] A. Massuda, C. Roques-Carmes, Y. Yang, S. E. Kooi, Y. Yang, C. Murdia, K. K. Berggren, I. Kaminer, and M. Soljačić, Smith–Purcell radiation from low-energy electrons, ACS Photonics **5**, 3513 (2018).
[26] F. J. García de Abajo, Optical excitations in electron microscopy, Rev. Mod. Phys. **82**, 209 (2010).
[27] N. Talebi, *Near-Field-Mediated Photon–Electron Interactions* (Springer International Publishing, Cham, 2019).
[28] A. Polman, M. Kociak, and F. J. García de Abajo, Electron-beam spectroscopy for nanophotonics, Nat. Mater. (2019).
[29] K. E. Echternkamp, A. Feist, S. Schäfer, and C. Ropers, Ramsey-type phase control of free-electron beams, Nat. Phys. **12**, 1000 (2016).
[30] K. E. Priebe, C. Rathje, S. V. Yalunin, T. Hohage, A. Feist, S. Schäfer, and C. Ropers, Attosecond electron pulse trains and quantum state reconstruction in ultrafast transmission electron microscopy, Nat. Photonics **11**, 793 (2017).
[31] A. Feist, S. V. Yalunin, S. Schäfer, and C. Ropers, High-purity free-electron momentum states prepared by three-dimensional optical phase modulation, Phys. Rev. Research **2**, 0043227 (2020).
[32] N. Schönenberger, A. Mittelbach, P. Yousefi, J. McNeur, U. Niedermayer, and P. Hommelhoff, Generation and Characterization of Attosecond Microbunched Electron Pulse Trains via Dielectric Laser Acceleration, Phys. Rev. Lett. **123**, 264803 (2019).
[33] D. S. Black, U. Niedermayer, Y. Miao, Z. Zhao, O. Solgaard, R. L. Byer, and K. J. Leedle, Net Acceleration and Direct Measurement of Attosecond Electron Pulses in a Silicon Dielectric Laser Accelerator, Phys. Rev. Lett. **123**, 264802 (2019).
[34] A. Khursheed, N. Karuppiah, M. Osterberg, and J. T. L. Thong, Add-on transmission attachments for the scanning electron microscope, Rev. Sci. Instrum. **74**, 134 (2003).
[35] Y. Yamazawa, S. Okada, Z. Yasenjiang, T. Sunaoshi, and K. Kaji, The first results of the low voltage cold-FE SEM/STEM system equipped with EELS, Microsc. Microanal. **22**, 50 (2016).
[36] N. Brodusch, H. Demers, A. Gellé, A. Moores, and R. Gauvin, Electron energy-loss spectroscopy (EELS) with a cold-field emission scanning electron microscope at low accelerating voltage in transmission mode, Ultramicroscopy **203**, 21 (2019).
[37] K. Tsuno and E. Munro, Design of an omega filter for a 200 kV electron microscope, Rev. Sci. Instrum. **68**, 109 (1997).
[38] See Supplemental Material at http://link.aps.org/supplemental/10.1103/PhysRevLett.128.235301 for details, which includes Ref. [39–41].
[39] M. Kozák, J. McNeur, N. Schönenberger, J. Illmer, A. Li, A. Tafel, P. Yousefi, T. Eckstein, and P. Hommelhoff, , J. Appl. Phys. **124**, 023104 (2018).
[40] http://www.lumerical.com/, Ansys Lumerical FDTD.
[41] M. Solà Garcia, Electron-matter interaction probed with time-resolved cathodoluminescence, Ph.D. thesis, AMOLF, 2021.
[42] Y. Adiv, K. Wang, R. Dahan, P. Broaddus, Y. Miao, D. Black, K. Leedle, R. L. Byer, O. Solgaard, R. J. England, I. Kaminer, J. England, I. Kaminer, J. England, and

I. Kaminer, Quantum Nature of Dielectric Laser Accelerators, Phys. Rev. X **11**, 041042 (2021).

[43] T. Sunaoshi, K. Kaji, Y. Orai, C. T. Schamp, and E. Voelkl, STEM/SEM, chemical analysis, atomic resolution and surface imaging at $\leq$ 30 kV with no aberration correction for nanomaterials on graphene support, Microsc. Microanal. **22**, 604 (2016).

[44] E. J. VandenBussche and D. J. Flannigan, Reducing radiation damage in soft matter with femtosecond-timed single-electron packets, Nano Lett. **19**, 6687 (2019).

[45] T. Sunaoshi, M. Shirai, S. Okada, K. Kaji, and E. Voelkl, Energy filtered STEM imaging at 30 kV and below—A new window into the nano-world?, Microsc. Microanal. **23**, 1560 (2017).

[46] O. Reinhardt, C. Mechel, M. Lynch, and I. Kaminer, Free-electron qubits, Ann. Phys. (Amsterdam) **533**, 2000254 (2021).

[47] T. R. Harvey, J.-W. Henke, O. Kfir, H. Lourenço-Martins, A. Feist, F. J. García de Abajo, and C. Ropers, Probing chirality with inelastic electron-light scattering, Nano Lett. **20**, 4377 (2020).

[48] A. Gover and A. Yariv, Free-Electron–Bound-Electron Resonant Interaction, Phys. Rev. Lett. **124**, 064801 (2020).

[49] R. Ruimy, A. Gorlach, C. Mechel, N. Rivera, and I. Kaminer, Toward Atomic-Resolution Quantum Measurements with Coherently Shaped Free Electrons, Phys. Rev. Lett. **126**, 233403 (2021).

[50] Z. Zhao, X.-Q. Sun, and S. Fan, Quantum Entanglement and Modulation Enhancement of Free-Electron–Bound-Electron Interaction, Phys. Rev. Lett. **126**, 233402 (2021).

[51] M. B. Lundeberg, Y. Gao, R. Asgari, C. Tan, B. Van Duppen, M. Autore, P. Alonso-González, A. Woessner, K. Watanabe, T. Taniguchi *et al.*, Tuning quantum nonlocal effects in graphene plasmonics, Science **357**, 187 (2017).

[52] I. Epstein, D. Alcaraz, Z. Huang, V.-V. Pusapati, J.-P. Hugonin, K. Avinash, X. M. Deputy, K. Tymofiy, T. G. Rappoport, J.-Y. Hong *et al.*, Far-field excitation of single graphene plasmon cavities with ultracompressed mode volumes, Science **368**, 1219 (2020).